Supplementary Material for
Electromagnetically induced transparency and wide-band wavelength conversion in silicon nitride microdisk optomechanical resonators

Yuxiang Liu,[1,2,*] Marcelo Davanço,[1,3,*] Vladimir Aksyuk,[1] and Kartik Srinivasan[1,†]

[1] *Center for Nanoscale Science and Technology, National Institute of Standards and Technology, Gaithersburg, MD 20899, USA*
[2] *Institute for Research in Electronics and Applied Physics, University of Maryland, College Park, MD 20742, USA*
[3] *Department of Applied Physics, California Institute of Technology, Pasadena, CA 91125, USA*

(Dated: April 16, 2013)

FINITE ELEMENT SIMULATIONS

We performed finite element method simulations of our microdisk structures to gain a clearer physical understanding of the optomechanical system.

Obtaining optical and mechanical cavity modes

Our microdisk cavities support whispering-gallery optical modes (WGMs) of the form $\mathbf{E}(r,z)\exp(im\phi)$, where $\mathbf{E}(r)$ is the electric field distribution on the rz plane (in cylindrical spatial coordinates) and m is the azimuthal order. Such WGMs were calculated by solving the 2D axially-symmetric electromagnetic wave equation

$$\nabla \times \nabla \times \mathbf{E} = \varepsilon(\mathbf{r}) \left(\frac{\omega}{c}\right)^2 \mathbf{E}. \tag{S1}$$

via the finite element method, with a formulation that employed respectively edge and node elements for the transverse and longitudinal electric field components, and perfectly-matched layers to simulate open boundaries. Solving the eigenvalue problem in eq. (S1) for a specific azimuthal order m produced eigenmodes with complex frequencies ω_m and optical quality factors $Q_m = \mathrm{Re}\{\omega_m\}/(2\mathrm{Im}\{\omega_m\})$. Because WGM fields are mostly concentrated in the periphery of the resonator, interaction with the Si pedestal that supports the SiN microdisk is negligible, and thus completely ignored in the optical mode calculation.

For disk radius $D \approx 10$ μm and SiN thickness $t \approx 350$ nm, modes with radiation-limited quality factors exceeding 10^8 can be found both in the 980 nm and 1300 nm bands. Table I shows wavelengths and quality factors of the calculated TE and TM polarized WGMs, which correspond well with experiment. The good agreement between the experimental and calculated values was achieved by tuning the parameters of the cavity within reasonable bounds (thickness $t = 340$ nm and $n = 1.99$ for the refractive index of SiN), compared to experimentally estimated values.

TABLE I. Calculated and experimental whispering gallery modes

λ_{FEM} (nm)	$Q_{\mathrm{o,FEM}} \times 10^8$	Polarization	$\lambda_{\mathrm{exp.}}$ (nm)
971.28	10	TE	970
987.37	4.5	TE	984
975.36	5.7	TM	974
989.61	2.4	TE	990
1281.23	1.0	TE	1285
1309.04	0.5	TE	1308

The mechanical modes of the microdisk structure were obtained by solving the equation of motion for the displacement field $\mathbf{Q}(\mathbf{r})$, assuming anisotropic materials [1]. In our simulations, the Si pedestal supporting the SiN microdisk was represented by a conical frustum whose angle and height were equivalent to those determined from scanning electron microscope images of fabricated structures. A zero displacement boundary condition was enforced at the bottom surface of the conical frustum, corresponding to the region where the pedestal meets the Si substrate.

For the 10 μm diameter disks considered, a first-order radial breathing mode (RBM) is obtained in the vicinity of f_m=625 MHz. The displacement profile of the RBM, as shown at the bottom of Fig. 1(e) (mode Ⓑ), is primarily in the radial direction and confined to the disk plane, with relatively small vertical displacement in the disk-pedestal contact area. Due to its azimuthal symmetry, the RBM is expected to display preferential optomechanical coupling to the microdisk's WGMs.

Optomechanical coupling

The shift in the frequency ω_o of a particular optical resonance due to displacement of the nanostructure boundaries produced by a mechanical resonance at frequency f_m is quantified by the optomechanical coupling $g_{om} = \partial\omega_o/\partial x = \omega_o/L_{\mathrm{OM}}$; here, x is the cavity boundary displacement and L_{OM} is an effective optomechanical interaction length [1]. The effective length L_{OM} can be estimated via the perturbative ex-

* These authors contributed equally
† kartik.srinivasan@nist.gov

TABLE II. Optomechanical coupling parameters between 980 nm and 1300 nm TE-polarized WGMs and 625 MHz RBM

λ_o (nm)	$Q_o \times 10^8$	$g_{om}/2\pi$ (GHz/nm)	$g_0/2\pi$ (kHz)	L_{om} (μm)
988.41	4.8	42.7	19.9	7.10
1281.80	1.0	33.2	15.5	7.05

pression

$$L_{\mathrm{OM}} = \frac{2\int dV \varepsilon |\mathbf{E}|^2}{\int dA\,(\mathbf{Q}\cdot\mathbf{n})\left(\Delta\varepsilon\left|\mathbf{E}_{\parallel}\right|^2 - \Delta(\varepsilon^{-1})\left|\mathbf{D}_{\perp}\right|^2\right)}. \tag{S2}$$

Here, $\mathbf{E}$ and $\mathbf{D}$ are the modal electric and electric displacement fields, respectively, $\Delta\varepsilon = \varepsilon_{diel.} - \varepsilon_{air}$, $\Delta(\varepsilon^{-1}) = \varepsilon_{diel.}^{-1} - \varepsilon_{air}^{-1}$, and $\varepsilon_{diel.}$ and ε_{air} are the permittivities of the microdisk material and air, respectively. The mass displacement due to the mechanical resonance is given by $\mathbf{Q}$, and the normal surface displacement at the structure boundaries is $\mathbf{Q}\cdot\mathbf{n}$, where $\mathbf{n}$ is the surface normal. The integral in the denominator is performed over the entire surface of the nanostructure.

The optomechanical coupling g_{om} can be converted into a pure coupling rate g_0 between the optical and mechanical resonances, with $g_0 = x_{zpf}\cdot g_{om}$, where $x_{zpf} = \sqrt{\hbar/2m\omega_m}$ is the zero point fluctuation amplitude for mechanical displacement and m is the motional mass of the mechanical resonance at frequency ω_m. The motional mass can be obtained from the displacement $\mathbf{Q}$ and the nanobeam material density ρ by $m = \rho\int dV\left(\frac{|\mathbf{Q}|}{\max(|\mathbf{Q}|)}\right)^2$ [2].

For the RBM at $f_m \approx 625$ MHz above, $m \approx 60$ pg and $x_{zpf} \approx 0.5$ fm. Table II shows calculated values of L_{om}, g_{om} and the zero-point coupling rate g_0 between the RBM and TE-polarized WGMs in both the 980 nm and 1300 nm bands. The calculated g_{om} values are smaller than those estimated via the expression $g_{om} = \omega_o/R$, with ω_o the optical mode frequency and R the disk radius, which is commonly employed for the case of large disks. For smaller radius disks such as considered here, optical fields extend considerably into the vacuum regions surrounding the dielectric, resulting in an effective optomechanical length L_{om} larger than the actual physical dimension R, as seen in Table II.

Clamping losses

To estimate mechanical clamping losses of the mechanical resonances, we adopted the method of ref. [3], in which the contact region between the disk and the pedestal is modeled as a membrane that radiates acoustic energy with power

$$P = c\rho\Omega_m^2\int_A dA\,|\mathbf{Q}(\mathbf{r})\cdot\hat{\mathbf{z}}|^2, \tag{S3}$$

where ρ is the density of the disk material and c is the speed of sound, Ω_m is the angular frequency of the mechanical resonance, and $|\mathbf{Q}(\mathbf{r})\cdot\hat{\mathbf{z}}|^2$ is the out-of-disk-plane displacement over the contact area A. If W_{mech} is the stored mechanical energy of the resonance, the latter's mechanical quality factor can be estimated as

$$Q_{\mathrm{m}} = \left(\frac{P}{\Omega_m W_{mech}}\right)^{-1}. \tag{S4}$$

Assuming a conical frustum for the pedestal shape, we calculate mechanical modes as a function of pedestal radius at the interface with Si_3N_4 (Fig. 1(e) top), with displacement amplitude profiles shown for two modes at a radius of 500 nm (Fig. 1(e) bottom). We also plot the mechanical mode frequencies and Qs due to clamping losses, following the approach of Anetsberger et al. [3]. It is apparent in Fig. 1(e) that, for large top pedestal radius, the mechanical quality factor for the RBM tends to decrease with increasing pedestal radius, a result of the increased contact area through which energy may radiate. At the same time, for a contact areas with radius near 200 nm, the RBM mixes with a secondary ('pedestal') mode that displays a large vertical displacement at the disk center, as observed in the profile of mode Ⓐ. Such mixing is evidenced by an anti-crossing between the green and blue mechanical frequency curves in Fig. 1(e), and by a steep decrease in quality factor in the neighborhood of the anti-crossing. Reduced quality factors in this range are associated with the relatively large vertical displacement of the pedestal mode. For radii below 200 nm the RBM quality factor increases again (green curve in Fig. 1(e)), as the pedestal mode is driven towards lower frequencies.

While the geometrical details of the Si pedestal must be included for an exact determination of the pedestal mode frequencies, we have observed that, generally, smaller pedestal top radii were necessary to ensure that such modes would be

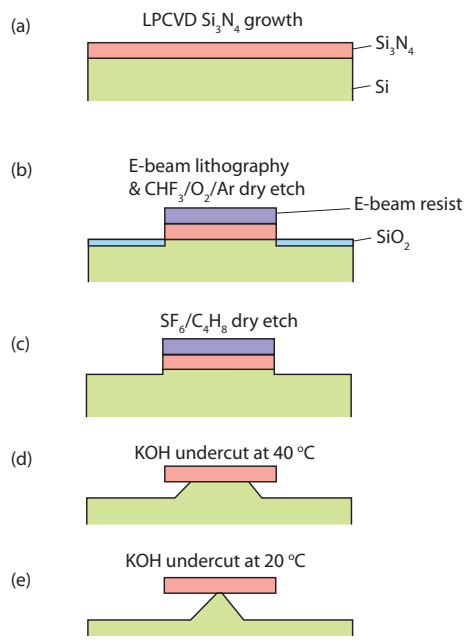

FIG. S1. Processing steps for fabrication of the Si_3N_4 microdisks.

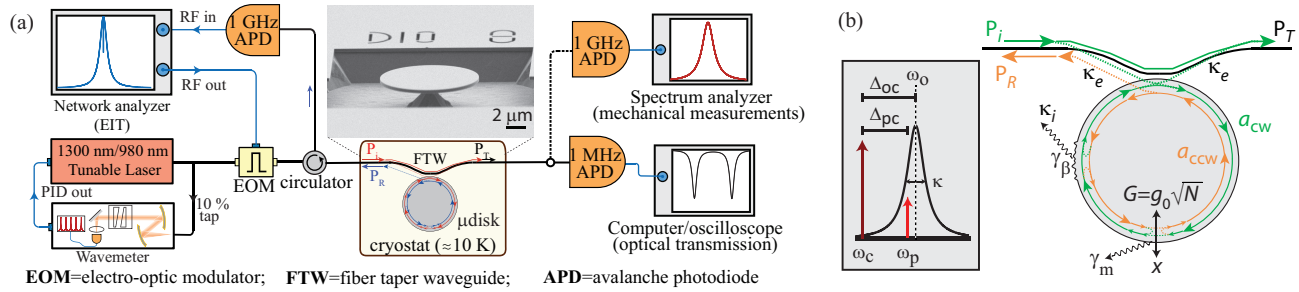

FIG. S2. (a) Schematic of experimental setup for EIT measurements. (b) (Left) Sideband spectroscopy schematic. (Right) Schematic of the microdisk with the optical whispering gallery modes and optical and mechanical coupling mechanisms. $a_{\rm cw}/a_{\rm ccw}$ are amplitudes for clockwise/counterclockwise (cw/ccw) optical modes, which couple to the radial breathing mechanical mode (amplitude x) at a rate g_0 that is parametrically-enhanced to a rate G through an optical control field (at $\omega_{\rm c}$) that injects N photons into the cavity. κ_i and κ_e are the intrinsic optical loss and waveguide-cavity optical coupling rates, respectively, $\gamma_{\rm m}$ is the mechanical damping rate, and γ_β is a backscattering rate that couples the cw and ccw optical modes. $P_i/P_R/P_T$ are the incident, reflected, and transmitted optical powers through the FTW.

out of the range of the RBM. Our highest mechanical quality factors ($Q_m \approx 1\times10^4$) were measured for a pedestal radius of 100 nm, which is essentially the smallest size that we can produce with our current fabrication process, where the theoretical value is $Q_m \approx 4\times10^4$.

DEVICE FABRICATION

The device fabrication started with a bare silicon wafer, as shown in Fig. S1. A layer of 350 nm thick stoichiometric Si_3N_4 was grown by low pressure chemical vapor deposition (LPCVD), with a process-induced internal tensile stress of $\approx$ 800 MPa, as measured by the wafer bowing method. A 500 nm thick positive-tone electron beam (E-beam) resist was spin-coated on the Si_3N_4 film, followed by E-beam lithography and development in hexyl acetate at 8 °C. The patterns were then transferred into the Si_3N_4 layer by an $O_2/CHF_3/Ar$ inductively-coupled plasma reactive ion etch (RIE). This RIE step apparently leaves a thin layer of SiO_2 on top of the exposed Si surface, preventing any subsequent KOH undercut (Fig. S1(b)). To rectify this, before the e-beam resist was removed, an additional SF_6/C_4F_8 inductively-coupled plasma RIE was carried out to remove the SiO_2 layer (as well as some Si), while the residual E-beam resist protected the Si_3N_4 device layer. After resist removal using a stabilized H_2SO_4/H_2O_2 solution, the sample was undercut in a 20 % KOH bath, as this concentration has an etch rate that is relatively insensitive to temperature fluctuations. The KOH etch was performed in two steps to achieve a small ($\lesssim$ 200 nm) top pedestal diameter under the microdisk. We started to etch the sample at 40 °C to quickly remove the bulk Si, with periodic inspection of the pedestal size under an optical microscope every 6 to 10 minutes. When the pedestal size was less than 1 μm, the undercut was continued at a temperature of 20 °C to reduce the etch rate. The undercut was stopped every 4 minutes for inspection, until one or more microdisks were completely released (etch rate variations across the chip prevent all devices from being completely released for the same undercut time). The pedestal diameters for the remaining (intact) microdisks were typically $\lesssim$200 nm, as determined by imaging with a scanning electron microscope.

EIT EXPERIMENTAL SETUP

The experimental setup for device characterization and EIT measurements is shown in Fig. S2(a). Light from a 1300 nm or 980 nm band tunable diode laser is coupled to the devices using an optical fiber taper waveguide (FTW). Optical modes are measured by sweeping the laser wavelength and recording the transmitted signal through the FTW. Mechanical modes are measured with the laser wavelength tuned to the shoulder of an optical mode. The transmitted optical power, which fluctuates due to the disk mechanical motion, is spectrally resolved on a real-time electronic spectrum analyzer. Increasing the optical power from $\approx$ 0.2 μW to higher powers when the laser is blue-detuned with respect to the cavity mode results in a narrowing of $Q_{\rm m}$ by over an order of magnitude (Fig. 1(d)), as the laser drives the system into regenerative oscillations [4]. On the other hand, strong pumping on the red-detuned side of the cavity is limited by instability due to thermo-optic effects. Mitigation of this thermo-optic instability is the primary reason why the EIT and wavelength conversion measurements presented in this paper are conducted with the sample housed in a liquid helium flow cryostat.

In EIT measurements, the probe is derived from the control field using an electro-optic amplitude modulator (EOM) to generate higher and lower frequency sidebands, only one of which is coupled into the cavity since it operates in the resolved sideband limit (Fig. S2(b)). The EOM is driven by a network analyzer, with the modulation frequency swept to vary the probe-control beam detuning $\Delta_{\rm pc} = \omega_{\rm p} - \omega_{\rm c}$. This results in sweeping the probe wavelength across the optical cavity mode when the the control wavelength is fixed. The probe and control fields pass through a circulator before going to the device, whose reflected signal is demodulated by the network analyzer to monitor the change of reflected probe sig-

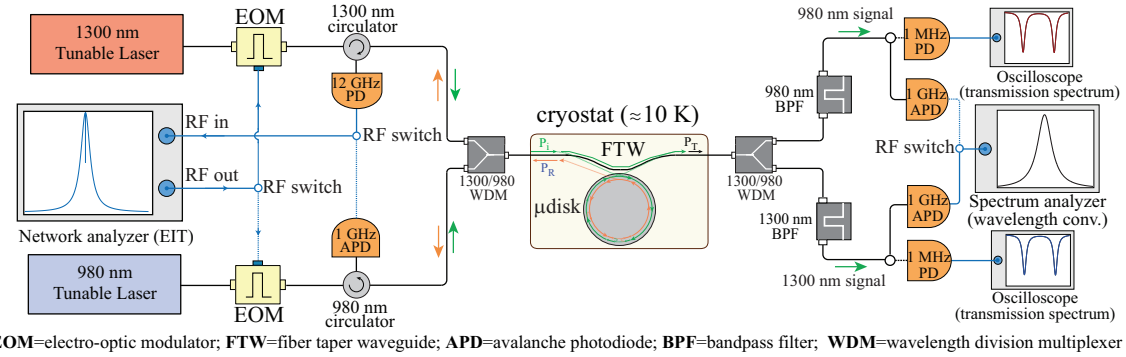

FIG. S3. Detailed schematic of the wide-band wavelength conversion experiment. EIT spectroscopy in the 1300 nm and 980 nm bands is performed on the reflected signal from the cavity, with fast switching between the two bands enabled by radio frequency (RF) switches. In frequency upconversion (downconversion), the 1300 nm (980 nm) laser is modulated to generate an input probe signal field, which is converted to the 980 nm (1300 nm) band through application of the 980 nm (1300 nm) control field. The frequency converted field transmitted past the cavity is measured on the RF spectrum analyzer.

nal during the sweep of the probe signal. A wavemeter tracks the control field wavelength and is used in feedback to lock Δ_{oc} (see section below).

LOCKING OF Δ_{oc}

In EIT experiments, the microdisk cavity is heated when the control laser reaches high power levels, resulting in a red-shift of the resonances due to the thermo-optic effect. It is thus difficult to maintain a fixed detuning (Δ_{oc}) between the control field and optical cavity without feedback. To reduce this instability, we lock Δ_{oc} by adjusting the control laser wavelength to track the red-shifted cavity resonance, following a procedure similar to that outlined in [5]. First, a small portion of the control field is split off and fed to a wavemeter (Fig. S2) equipped with a PID controller whose output is fed back to the laser to fix its absolute wavelength at a specified value. This specified value is determined by sweeping Δ_{pc} over a broad frequency range (0 to 3 GHz) and fitting the acquired data by the vector network analyzer to determine the real value of Δ_{oc}. The control field wavelength is then adjusted to ensure that the desired Δ_{oc} is achieved, and the process repeated until the fit value of Δ_{oc} remains stable over several scans in a row. Typical locking times are on the order of a few seconds (for lower powers) up to a couple tens of seconds (for the highest powers). Power levels beyond that shown in Fig. 2 result in thermally unstable behavior, where the cavity mode shifts too far away from the control laser for the above approach to be effectively applied.

Once the locking procedure kept Δ_{oc} within a predetermined acceptable range around the target value (e.g., 50 MHz), EIT measurements consist of sweeps of Δ_{pc} recorded over two frequency ranges - the first over a broad range to provide an overall picture of the cavity reflection spectrum, and the second over a narrow range to record the details of the EIT dip. For each set of parameters (optical powers and Δ_{oc}), these sweeps were repeated 16 times and the data plotted in Fig. 2 is an average of these scans.

WAVELENGTH CONVERSION EXPERIMENTAL SETUP

In frequency upconversion (downconversion), a 1285 nm (990 nm) control pump laser is modulated to generate an input probe signal field in a similar fashion to the EIT experiments. The input probe is then upconverted (downconverted) through application of a 990 nm (1285 nm) control pump field. The detuning between input probe field and 1285 nm (990 nm) control pump is swept to assess the bandwidth of the conversion process.

The detailed setup used for wavelength conversion experiments is shown in Fig. S3. The following discussion is based on the upconversion process, while a similar explanation can be readily applied to downconversion by swapping the input signal and converted signal wavelengths. As in Fig. S2, EIT spectroscopy in the 1300 nm and 980 nm bands is performed on the reflected signal from the cavity. Fast switching between the two bands is enabled by RF switches, and the main results of the EIT measurements are to determine Δ_{oc} and the cooperativity achieved for each mode. Wavelength conversion experiments proceed by combining the input 1285 nm probe field

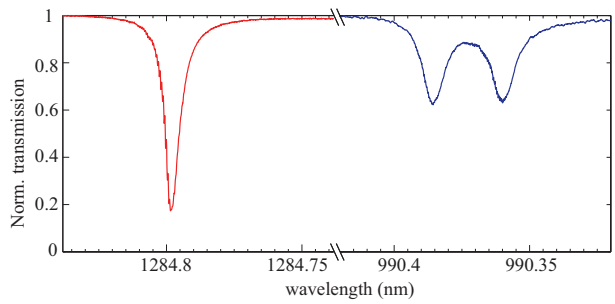

FIG. S4. Measured optical spectra of the two modes, one at 990 nm and the other at 1285 nm, in the wavelength conversion experiment.

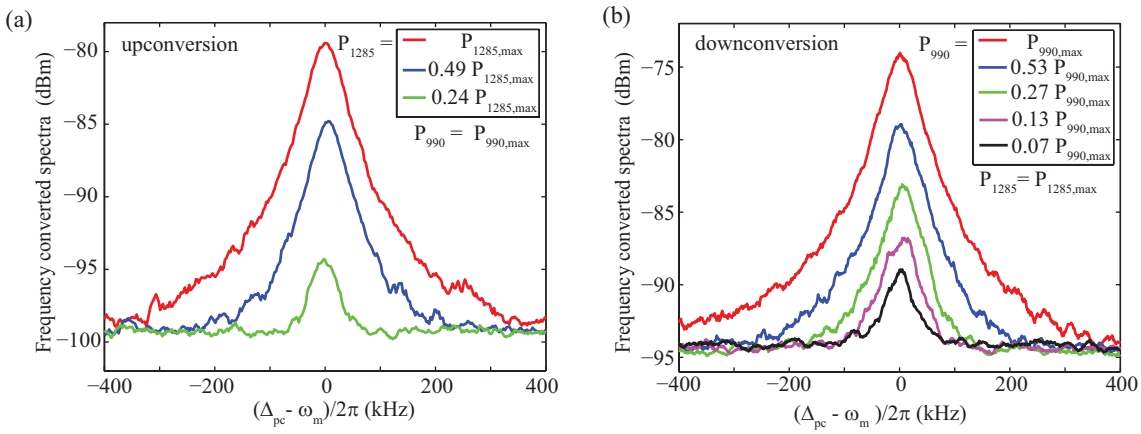

FIG. S5. (a) Upconversion signals (990 nm) measured at different optical powers of the 1285 nm control field at the device input. (b) Downconversion signals (1285 nm) measured at different optical powers of the 990 nm control field. In upconversion (downconversion), the 990 nm (1285 nm) control field power is fixed at $P_{990,\mathrm{max}}$=9.0 μW ($P_{1285,\mathrm{max}}$=63.8 μW) and the 1285 nm (990 nm) control field power is stepped.

with the control fields in both the 980 nm and 1300 nm bands using a wavelength division multiplexer (WDM) before being sent into the device. Light exiting the optomechanical system is spectrally separated into the 980 nm and 1300 nm bands using a WDM and bandpass filters (BPFs), and the converted 990 nm signal is detected by a 1 GHz APD whose output is recorded by a real-time electronic spectrum analyzer. The input probe wavelength (near 1285 nm) is swept while the control wavelengths in both bands are fixed, which results in a sweep of the generated probe signal at the conversion wavelength (990 nm). The transmitted converted signal at 990 nm is measured by the spectrum analyzer. This measured signal is the result of interference between the 990 nm pump, which is constant in both power and wavelength, and the converted 990 nm probe. As sweeping of the 1285 nm input probe signal results in a sweep of the converted 990 nm tone, we are able to assess the dependence of the conversion efficiency on the input signal-control detuning (Δ_{pc}) at 1285 nm. Each curve shown in Fig. 3(c) is the envelope of $\approx$ 10 swept traces of the measured signal at 990 nm.

WAVELENGTH CONVERSION MEASUREMENTS

In wavelength conversion experiments, the RF spectrum analyzer measures a signal that results from the interference of the converted probe signal with the control pump situated in the same wavelength band (and which is detuned by a mechanical frequency ω_{m}). Considering the case of upconversion from 1285 nm to 990 nm, the optical power measured by the AC-coupled APD is proportional to $\sqrt{P_{990,\mathrm{conv}}P_{990}}$, where $P_{990,\mathrm{conv}}$ is the wavelength-converted probe signal and P_{990} is the control pump power. The APD detector converts this to a voltage, and the RF spectrum analyzer measures an RF power proportional to the square of this voltage, that is, proportional to $P_{990,\mathrm{conv}}P_{990}$. Next, we can write $P_{990,\mathrm{conv}} = \eta_{\mathrm{up}}P_{1285,\mathrm{input}}\omega_{990}/\omega_{1285}$, where $P_{1285,\mathrm{input}}$ is the input probe signal power, ω_{990} (ω_{1285}) is the optical frequency at 990 nm (1285 nm), and η_{up} is the photon number conversion efficiency (the ratio of the converted signal photon number to the input signal photon number). Finally, because $P_{1285,\mathrm{input}}$ is created through modulation of the 1285 nm control field, the two are related by the modulation index β_{1285} as $P_{1285,\mathrm{input}} = \beta_{1285}^2 P_{1285}$, where P_{1285} is the 1285 nm control field power.

Putting this all together, we write the measured RF power at ω_{m} as:

$$H_{990} = \Re_{990}\eta_{\mathrm{up}}\beta_{1285}^2 P_{1285}P_{990}\frac{\omega_{990}}{\omega_{1285}}$$

$\Re_{990}$ is a constant that depends on the APD gain, responsivity, and load resistance.

A similar expression can be written in the case of frequency downconversion, swapping the roles of the 990 nm and 1285 nm bands, and using a prefactor $\Re_{1285}$ that depends on the detector response at 1285 nm. The efficiencies of upconversion and downconversion, η_{up} and η_{down}, can thus be determined from the RF spectra, control pump powers, optical frequencies, and input modulation indices.

WAVELENGTH CONVERSION DATA

The measured optical spectra of the two modes used in the wavelength conversion experiments is shown in Fig. S4. In comparison to Fig. 1 and 2, Q_{o} here is lower, with $\kappa/2\pi \approx$ 1 GHz and 3 GHz at 1285 nm and 990 nm, respectively. The increased losses are both due to additional sample degradation and the need to simultaneously achieve a reasonable coupling level to both optical modes (in Fig. 2, this was individually optimized).

Wavelength conversion measurements were taken as a function of detuning between the input probe and control field

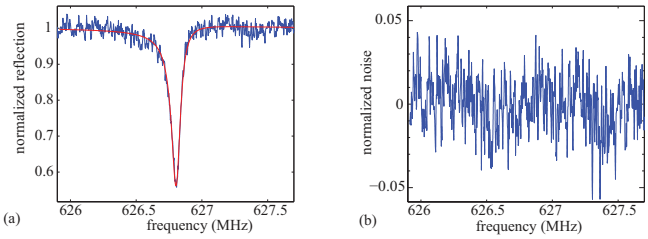

FIG. S6. (a) Raw data (blue) and the fitted curve (red) of the 1300 nm EIT signal at the control power of 21.9 μW. (b) Difference between the raw data and the fitted curve shown in (a).

within the same wavelength band (Δ_{pc}) and as a function of pump power for both control fields. Figure 3(c) shows the dependence of the converted signal on the control power in the converted wavelength band, while here we show the conversion dependence on the control power in the input signal band (Fig. S5). The acquired spectra are the result of interference of the converted probe signal and control pump in the conversion band, for different power levels of the control pump situated in the input signal band. Therefore, different from the results shown in Fig. 3(c), all the curves in each figure of Fig. S5 share the same noise floor level because the control pump power in the converted band is fixed.

FITTING THE DATA

Experimentally-measured optical transmission spectra are fit using coupled mode theory for a resonator-waveguide system. For single dips, this yields a Lorentzian function, while doublet modes are fit using a model that takes into account backscattering due to surface roughness, as described elsewhere [6, 7]. In the limit of large doublet spitting with respect to the cavity linewidths, a pair of Lorentzians can accurately fit the data. Mechanical spectra were fit with single Lorentzian functions.

Fitting of the EIT signals (Fig. 2(b)) is based on Eq. (1) from the main text, which we repeat here:

$$r(\Delta_{pc}) = -\frac{1}{1+\frac{2i(\Delta_{oc}-\Delta_{pc})}{\kappa}+\frac{C}{\frac{2i(\omega_m-\Delta_{pc})}{\gamma_m}+1}} \tag{S5}$$

The values of κ, Δ_{pc}, and Δ_{oc} were acquired from the broad scans of the EIT signal. The intracavity photon number is determined as:

$$N = \frac{1}{\hbar\omega_o}\sqrt{\xi}\Delta T Q_i(\frac{P_{in}}{\omega_o})\frac{1}{1+(\frac{\Delta_{oc}}{2\kappa})^2} \tag{S6}$$

where $\hbar$ is the Planck constant divided by 2π, ξ is the FTW transmission, ΔT is the depth of the optical resonance in the transmission spectrum (ΔT=1 at critical coupling), Q_i the intrinsic optical Q, and P_{in} is the optical power at the FTW input. We measured a background signal with the FTW far away from the device to account for the frequency-dependent response of the APD, EOM, and network analyzer. The fitting was carried out on the experimentally acquired EIT data divided by the background signal.

The fitting of the EIT width versus control power (inset in Fig. 2(c)) is based on the expression for the total mechanical damping rate $\gamma = \gamma_m(1+C)$. The fitted value of g_0 from the EIT width is approximate equal to that obtained from the EIT depth fitting, with an error of ≈ 6 %.

UNCERTAINTY ESTIMATES

The error bars in Fig. 2(c) arise from the noise of recorded raw EIT data. By subtracting the fitted curve from the raw EIT data (Fig. S6(a)), we obtained the noise of the EIT signal (Fig. S6(b)). The one standard deviation value of this noise signal is considered as the uncertainty of the EIT signal depth and is plotted as the error bar in Fig. 2(c). By combining the uncertainty of the reflected EIT signal and the slopes of the fitted curves at both the left and right shoulders, we obtained the uncertainty of the width of the EIT signal. This width uncertainty is plotted as the error bars in the inset figure of EIT width versus the optical power in Fig. 2(c).

The uncertainty in Q_m shown in Fig. 1(d) is given by the 95 % confidence intervals of the Lorentzian curve fitting of the experimentally measured mechanical spectra.

[1] M. Eichenfield, J. Chan, R. M. Camacho, K. J. Vahala, and O. Painter, Nature **462**, 78 (2009).
[2] A. H. Safavi-Naeini and O. Painter, New Journal of Physics **13**, 013017 (2011).
[3] G. Anetsberger, R. Rivière, A. Schliesser, O. Arcizet, and T. J. Kippenberg, Nature Photonics **2**, 627 (2008).
[4] T. J. Kippenberg and K. J. Vahala, Science **321**, 1172 (2008).
[5] J. Chan, *Laser cooling of an optomechanical crystal resonator to its quantum ground state of motion*, Ph.D. thesis, California Institute of Technology (2012).
[6] M. Borselli, K. Srinivasan, P. E. Barclay, and O. Painter, Appl. Phys. Lett. **85**, 3693 (2004).
[7] T. J. Kippenberg, S. M. Spillane, and K. J. Vahala, Opt. Lett. **27**, 1669 (2002).